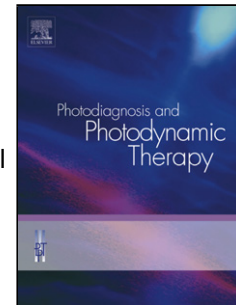


# Journal Pre-proof

Tissue Characterization Utilizing Hyperspectral Imaging for Liver Thermal Ablation

Mohamed Hisham Aref (Conceptualization) (Formal analysis) (Investigation) (Methodology) (Resources) (Writing - original draft) (Writing - review and editing), Ibrahim H. Aboughaleb (Conceptualization) (Formal analysis) (Investigation) (Methodology) (Resources) (Writing - original draft) (Writing - review and editing), Yasser H. El-Sharkawy (Conceptualization) (Methodology) (Supervision) (Writing - review and editing)



PII: S1572-1000(20)30253-2

DOI: <https://doi.org/10.1016/j.pdpdt.2020.101899>

Reference: PDPDT 101899

To appear in: *Photodiagnosis and Photodynamic Therapy*

Received Date: 23 March 2020

Revised Date: 20 June 2020

Accepted Date: 22 June 2020

Please cite this article as: Aref MH, Aboughaleb IH, El-Sharkawy YH, Tissue Characterization Utilizing Hyperspectral Imaging for Liver Thermal Ablation, *Photodiagnosis and Photodynamic Therapy* (2020), doi: <https://doi.org/10.1016/j.pdpdt.2020.101899>

This is a PDF file of an article that has undergone enhancements after acceptance, such as the addition of a cover page and metadata, and formatting for readability, but it is not yet the definitive version of record. This version will undergo additional copyediting, typesetting and review before it is published in its final form, but we are providing this version to give early visibility of the article. Please note that, during the production process, errors may be discovered which could affect the content, and all legal disclaimers that apply to the journal pertain.

© 2020 Published by Elsevier.

# Tissue Characterization Utilizing Hyperspectral Imaging for Liver Thermal Ablation

Mohamed Hisham Aref\* Mh-aref@ieee.org, Ibrahim H. Aboughaleb, and Yasser H. El-Sharkawy

Biomedical Engineering Department, Military Technical College, Cairo, Egypt

\* Corresponding author; Tel.: +20-0122-1997009

## Highlights

- Hyperspectral imaging (HSI) is an emerging modality for the monitoring of thermal liver ablation.
- The diffuse spectral reflectance at (720±18.92 nm) of *ex-vivo* bovine liver tissue after RF ablation process provides signature for thermal ablation monitoring of liver tissue.
- The custom optical imaging system with the associated K-means algorithm is a simple, accurate, and capable tool to monitor the thermal ablation.

## Abstract:

**Background:** Thermal ablation is the dominant modality to treat liver tumors for discriminating patients who are not allowed to have surgical intervention. Conversely observing or foreseeing the size of the subsequent tissue putrefaction during the Thermal Ablation techniques is a difficult undertaking.

**Objective:** To examine the impacts of ablation zone volume following Radiofrequency ablation (RFA) of an *ex-vivo* bovine liver to correlate the impacts of thermal ablation with target organ perfusion; by exploiting the unique properties of Hyperspectral Imaging (HSI).

**Materials and Methods:** Radiofrequency ablation was perfused on *ex-vivo* bovine livers at peripheral and central- vessel- adjacent locations, and monitored by HSI with a spectral range from 400 to 1000 nm. The system contains k-means clustering (K=8) algorithms combining spectral and spatial information. Labeled spectral signatures datasets were used as training data. Statistical analysis (10 samples) was computed to calculate the highest variance between six spectral images for determining the optimum wavelength for discrimination between the affected regions after thermal ablation (normal, thermal, and ablated liver tissue regions).

**RESULTS:** The change of the optical properties of *ex-vivo* liver tissues provides different responses to light transmission, scattering, absorption and particularly the reflection over the spectrum range. The produced spectral image from reflection with the highest variance (358.07) empowered us to determine the optimum wavelength spectral image (720±18.92 nm) to distinguish between the normal, ablated, and thermal categories.

**CONCLUSION:** Hyperspectral imaging is a powerful tool in monitoring tissue characterization, which is useful technique for edge evaluation of liver thermal ablation to enhance the surgical outcome.

**Keywords:** Liver Tumor; Hyperspectral Imaging; RF thermal Ablation; Spectral Diffuse Reflectance; K-mean clustering algorithm.

## 1. Introduction:

Liver malignancy is the 5<sup>th</sup> most common tumor and the 2<sup>nd</sup> most prominent reason for tumor-related passing around the world, more than (800,000) deaths are accounted for globally every year [1,2]. In Egypt, there has been a noteworthy increment in the extent of hepatocellular carcinoma (HCC) among interminable liver disease patients [3]. Hepatocellular carcinoma (HCC) is the most well-known essential dangerous tumor in the liver, particularly in patients with cirrhosis [4]. Confirmed patients with HCC follow a specific system for stage classifier and best treatment opportunity, such as the Barcelona Clinic Liver Cancer (BCLC) stage system [5].

Liver successful transplantation is considered the best option for HCC treatment for eligible patients [2,6,7]. However, transplantation is constrained by the accessibility of liver contributors and by the available budget, should also fulfill the Milan criteria [8]. Another great restorative alternative for initial-phase HCC patients with the non-cirrhotic liver is hepatic resection [9]. Fractional hepatectomy gives shorter holding up times and practically identical 5-year endurance rates (60~70%) contrasted with transplantation [10]. On the other hand, the number of colorectal metastases (CLM) patients qualified for resection is less than 20% because of incompatible tumor areas and worsened residual liver function [11].

Negligibly intrusive thermal ablation, including laser interstitial thermotherapy [12], radio-frequency Ablation (RFA) [13], microwave Ablation (MWA) [14,15], and high-Intensity ultrasound (US) (e.g., interstitial [16], Focused US [17], unfocused US [18]) and bulk thermal ablation [19,20]. All these modalities is a significant treatment way to deal with unresectable essential and secondary liver tumors (e.g., HCC and CLM) [13,18,21]. Where, All thermal ablation modalities plan to quickly raise the tissue temperature over 60 °C, resulting in thermal coagulative necrosis inside a zone incorporating all tumor edges.

Under typical conditions, normal human body temperature level is 37~ 42°C, No quantifiable impacts are observed covering this range. "Hyperthermia" extending from roughly 42.5~45°C, (*Cell proteins - both membrane and cytoplasmic proteins*) undergo conformational changes [22]. Further than 45°C, a quantifiable decrease in chemical movement is observed, subsequent about a decreased energy move inside the cell and fixed status of the cell itself. At 60°C, denaturation of proteins and collagen transpires which prompts coagulation of tissue and rot of cells. At 100°C, the water particles contained in many tissues begin to disintegrate. Because of the huge increment in volume during this stage progress, gas bubbles are shaped instigating mechanical bursts and warm deterioration of tissue parts [19,22,23], as more illustrated in Figure 1.

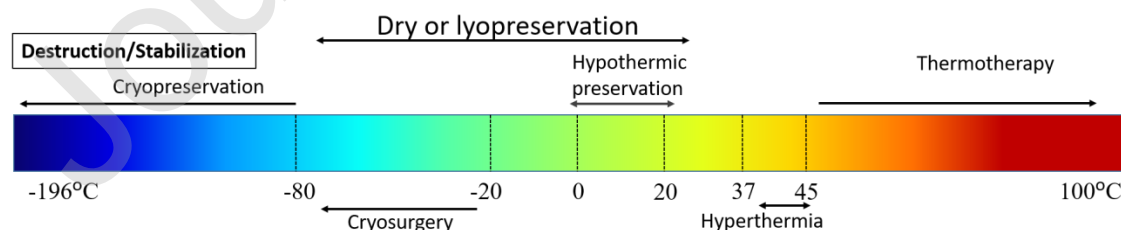


**Figure 1** - A Brief of Typical Thermal Effect on Thermostability of Biological Systems over a Wide Temperature Range (from the Cryogenic to Hyperthermic Temperatures).

Thermal ablation may likewise be utilized to help careful resection to diminish intraoperative blood loss and postoperative hospitalization [13]. While, it is considered being the most fitting alternative track for HCC long-suffering patients who are unqualified for both transplantation and resection. This track is usually used for the patients who have tumor size  $\leq 3$

cm, in light of the BCLC classification framework [5,13]. Thermal ablation may likewise give a 5-year generally survival rate identical to surgical resection (47.6% versus 56.0%) for patients with little CLM [24]. However, the serious issue of thermal ablation is incomplete ablation prompting ablation site recurrences (ASR), for which an unmistakable definition ought to be utilized [25,26].

Even-though, RF ablation is more affordable, less obtrusive, and with lower difficulty rates than incomplete resection in early hepatocellular carcinoma (HCC) and small colorectal metastases [27,28]. However, it is not the ideal modality due to the inability of monitoring the thermal effect accurately with the conventional image-guided techniques, such as Computed Tomography (CT) and Ultrasound (US) [29]. In particular, US would be the best choice for RF ablation real-time monitoring, due to its widespread availability, low cost, and real-time imaging high resolutions [17]. However, US can be hardly effective for the real-time monitoring due to the struggle of separation of feasible and destructed tissue and distinguishing proof of the tumor edges, as a result of tissue scarring and gas bubble fact which emerge during the thermal procedure [30,31]. Where, one of the previous studies shows that 48% of tumors close to large blood vessels were treated incompletely [32]. On the other hand, other research's result shows that 14% of RFA-treated malignant liver tumors developed local recurrence [33].

Recently, many researchers have developed several imaging methods to guarantee suitable removal of liver malignant and metastases utilizing non-intrusive or negligibly obtrusive systems with respect to the conventional excisional biopsy. Of these imaging techniques, the CT modality utilizing MWA (HS Medical, Amica™, F=2.45 GHz) with Ablation protocol (100 W 4.5 min) on three *ex-vivo* porcine samples, the outcomes showed ablation diameter ( $4.1 \pm 0.2 \times 5.6 \pm 0.2$ ) [34]. Other study combine both the US and CT utilizing MWA (KY-2000, Kangyou Medical, F=2.45 GHz) with Ablation protocol (50 W 10 min) on four *ex-vivo* calf livers, the results showed ablation diameter ( $2.1 \pm 0.1$  mm (15 markers used) [35]. A study using Contrast Enhanced Ultrasonography (CEUS) technique with Interstitial laser thermal therapy (ILTT) with Ablation protocol (15 W, 100 °C, 12 min) on 12-patient clinical trial, the results present ablation diameter (11~16 mm) [36]. Additionally, infrared thermography monitoring [37,38], real-time ultrasound elastography [39], high resolution US [39,40] and electrode vibration elastography [41].

This exploratory investigation was the leading at the attainability of HSI observing in RFA. On the other side hyperspectral imaging (HSI) method provides a specific wavelength (spectral image) across the electromagnetic spectrum as it collects spatial and spectral information for the specimen under investigation [42][43,44].

Spectral imaging is otherwise called imaging spectroscopy, which introduces the innovation that incorporates conventional imaging and spectroscopy techniques to acquire both spatial and spectral data of an object [45]. It was at first described in the late 1980s for remote distinguishing of the Earth [44]. Spectral imaging can be separated into multispectral imaging, hyperspectral imaging (HSI), as per its unearthly goals, the number of groups, width, and continuity of groups [46,47]. Multispectral imaging frameworks, for the most part, gather information in few and generally noncontiguous wide ghastly groups, regularly estimated in micrometers or several micrometers. These ghastly groups are chosen to gather power in explicitly characterized pieces of the range and advanced for specific classes of data generally clear in those groups. While HSI frameworks can gather many object groups [42,45].

HSI is a rising imaging methodology, and promising outcomes have been appeared as for malignant growth identification in the brain. Where, two HS camera is used covering the spectral range of 400~1700 nm, the system is able in ~1 min to discriminate between normal and malignant tissue in the brain tissue thru neurosurgical procedures [48]. Study on gastric tumors in

10 human subjects. Where, the spectral monograms were obtained and evaluated in normal and Tumor tissue. Processing methods with the standard deviation of the spectral graph, support vector machine, and the 1st derivatives were recommended to improve and detect the Tumor regions. The 1st derivatives in spectral region between 1226~1251 nm and 1288~1370 nm were suggested as criteria that successfully discriminate between normal and Tumor tissue [49].

Moreover, in the HSI in medical applications, ultrasonic thermos-elastic emissions were produced in breast tissue by the inclusion of nanosecond laser pulses at 1064 nm generated by a Q-switched Nd: YAG laser. Where the differences in photoacoustic reaction signatures of normal and malignant breast tissue were found to be highly enhanced [50]. In the prostate tumor, the HSI framework was utilized to catch *in-vivo* pictures of rats influenced by human prostate tumors. The results upon 11 mice proved that the sensitivity and specificity of the HSI classification technique are 92.8% to 2.0% and 96.9% to 1.3%, respectively [51].

This exploratory investigation was the leading at the attainability of HSI observing in RFA. On the other side, hyperspectral imaging (HSI) method provides a specific wavelengths (spectral image) across the electromagnetic spectrum as it collects spatial and spectral information for the specimen under investigation [42][43,44].

The measured optical spectra of biological tissues from 400 to 1000 nm cover the visible and NIR regions and can be broken down at the molecular level [52], which greatly contributes to the Diffuse Reflectance values measured in certain ranges according to the hemoglobin oxygenated and deoxygenated states [53,54]. Basics of tissue optics and photonics generally gave to biological tissue structures and their explicitness identified with light associations at its engendering in tissues [55][56]. There are several mechanisms due to the light-tissue interactions with the *ex-vivo* liver tissue sample, including (Absorption, Specular Reflectance, Diffuse Reflectance, Transmission, Diffuse Transmission) [57], depends on tissue optical properties of: (Tissue Type / density / size/ shape / color /refractive index) [57][55].

The change of the optical properties of liver tissue sample provides different responses to light transmission, reflection, absorption, and scattering over the spectrum range. Due to these properties, it can be identifying and characterized the investigated samples in a certain band by their spectral signature, as illustrated in Figure 2.

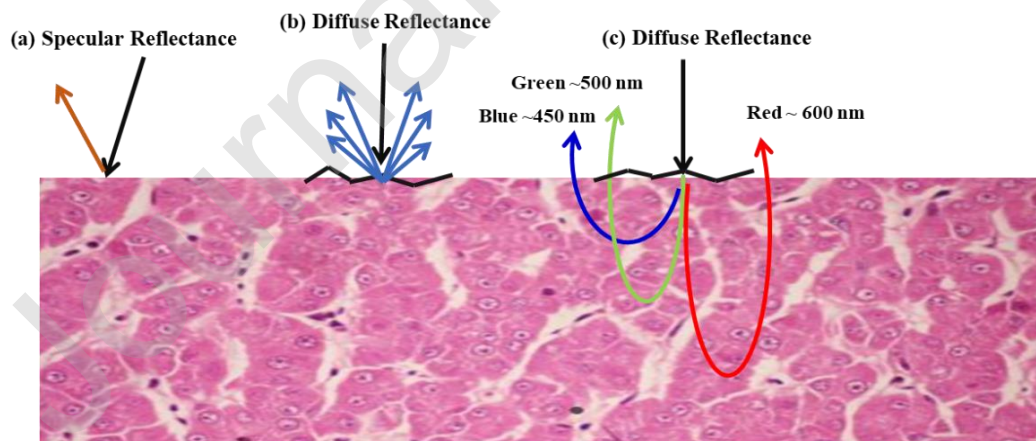


**Figure 2-** Some of the Light Interaction with the *ex-vivo* Bovine Liver Tissue Sample – (a) specular reflectance at smooth surface; (b) Diffuse Reflection from irregular surface without any absorption; (c) Diffuse Reflection from irregular surface with absorption at various wavelengths.

This pilot study demonstrates the objective of building and implementation a custom optical imaging system and associated K-mean clustering algorithm using to characterized and evaluate different thermal effects of investigated *ex-vivo* bovine liver samples. This non-invasive system can provide virtual information for a medical doctor, helping in early perception during surgery by improving tissue visibility and an early admonition to maintain a strategic distance



from tissue fibrosis and thermal impact utilizing electrosurgical generator or any other Surgery/Thermal ablation modality [50][58].

## 2. Materials and Methods:

In this sector, exploratory arrangement and techniques for a progression of examinations on controlled thermal ablation of *ex-vivo* Bovine liver tissue are talked about. In these analyses, where all the pieces of the framework and their interconnections are exhibited. Seven different elements compose the system acquisition platform for tissue characterization (Hyperspectral camera / CCD microscopic camera / Thermal camera / RF generator / Light source / Computer & its Image processing software / Liver sample posed on the white optical board).

### 2.1 Sample preparation:

Thermal removals were framed on freshly cut out bovine liver which was attained from a local abattoir in EGYPT and placed in ice-box with deionized saline, Liver tissue samples were crudely cut into (5×6 cm) chop. The analysis was performed at room temperature 25 °C, with a normal liver temperature of 23°C~25°C estimated before every preliminary and stored in refrigerator up to -70°C. A total of 20 ablations were executed in 10 different *ex-vivo* liver samples using an RF ablation system (BOWA; Arc303) and a 1.5 mm RF tip with 2.5 cm active blade length, as illustrated in Figure 3.

The terminal was embedded around 2 cm into the liver sample, and RF power (50 W) was applied for 1~3 mins utilizing the RF generator's impedance controlled power beating calculation to shape removals running in size from about 10 mm × 10 mm. All thermals were imaged inside 10 mins of thermal development utilizing HS imaging. Following data procurement, markers were embedded into the imaging plane on the two sides of the electrode, and the removal was cut through this plane and captured with the microscopic CCD camera; finally, the sample was scanned with individual scanner.

The necrosis areas generated by the RF generator (BOWA; Arc303) needle had been measured on the *ex-vivo* Bovine Liver, in order to verify their accordance with the expected area computed by the custom algorithm system. The ablation region with L-diameter (long ellipse diameter) of  $1.22 \pm 0.14$  cm, an S-diameter (short ellipse diameter) of  $0.44 \pm 0.09$  cm. Thermal#1 region with L-diameter of  $2.01 \pm 0.10$  cm, an S-diameter  $0.74 \pm 0.09$  cm. Thermal#2 region with L-diameter of  $2.61 \pm 0.12$  cm, an S-diameter  $1.1 \pm 0.11$  cm.

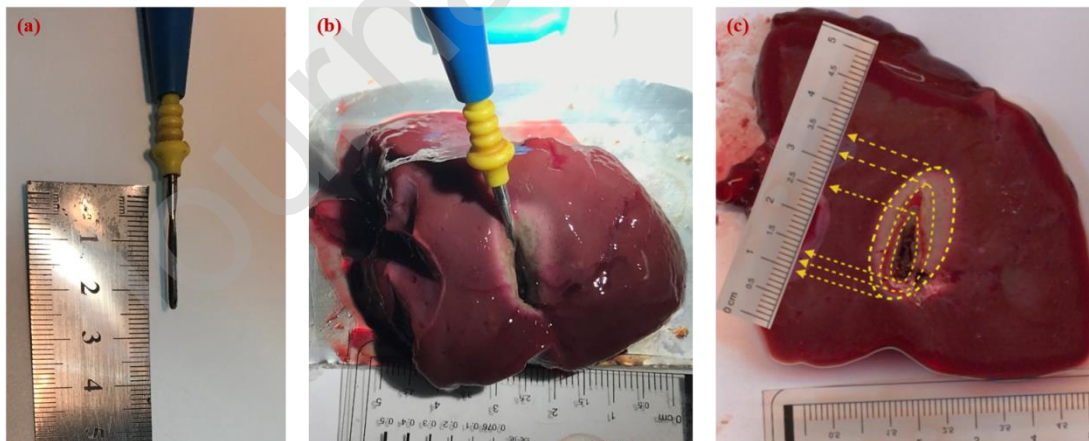


**Figure 3-** (a) Radiofrequency generator Tip; (b) The *ex-vivo* Bovine Liver Tissue Sample after ablation; (c) Plan view of *ex-vivo* Bovine Liver Tissue Sample after ablation highlighting the ablation, Thermal#1 and Thermal#2 zone region.

The size of each pixel exemplifies a tissue surface of  $0.22 \text{ mm} \times 0.22 \text{ mm}$ , the diffuse reflectance spectrum achieved with HS imaging originates from a much larger sampling volume. Therefore, the diffuse reflectance spectrum of a specific pixel might have been shaped by a different tissue type located at  $\leq 0.5 \text{ mm}$  distance.

## 2.2 Optical imaging system for liver sample ablation monitoring:

To capture the necessary Hyperspectral (HS) image data, we used HS Camera (Surface Optics, SOC710) this model has spectral range (400 to 1000 nm), 5 nm spectral resolution, pushbroom (line- scanning) and 10 degrees field of view. The camera incorporated with a lens (Schneider KREUZNACH XENOPLAN 1.9/35 CCTV-LENS 400 bis 1000nm). For each sample, the spectral cube image composed of 128 frames, and each frame represented a spectrum image of a specific wavelength.

HS cameras require solid and exact brightening of the scene to be caught so as to stay away from outside obstructions created by the ecological light where the catch is being performed. The enlightenment framework utilized a polychromatic light (Derungs, 20P SX -20 Watt) this model has a spectral range (400~950 nm). This sort of light is reasonable for HS applications because of the high homogeneity of its range over the whole spectral range and to discriminate the optimum wavelength for the tissue characterization, consequently utilizing Radiofrequency Generator (RF) (BOWA-Model: Arc303) was used to generate the necessary thermal ablation in the liver tissue and have been continuously monitored by the Non-Contact thermal camera (FLIR; ETS 320), as illustrated in Figure 4.

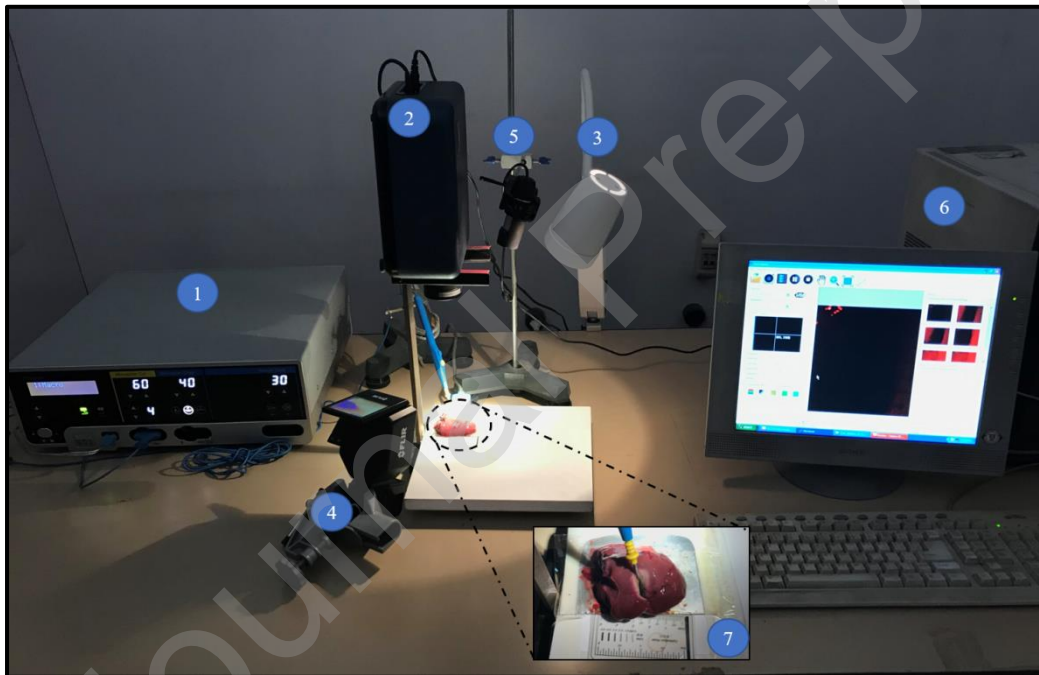


**Figure 4** –The Optical System to Monitor the Thermal Tissue characterization; (1) electrosurgical generator (BOWA-Model: Arc303), (2) Hyperspectral Camera (Surface Optics –Model: SOC710), (3) Polychromatic source light (Derungs –Model:20P SX -20W), (4) Thermal Camera (FLIR -Model: ETS 320), (5) CCD microscopic camera (500X), (6) Computer and software analysis, (7) Sample under test of Bovine Liver Tissue was posed on white optical board

## 2.3 Hyperspectral picture conquering:

HSI sensors produce a three-dimensional (3D) information structure, called HS block, where the spatial data is contained in the initial two measurements, while the third measurement incorporates the spectral data [59,60]. In a hyperspectral picture, every pixel has an arrangement of Diffuse Reflectance in various spectral frequencies that can show the spectral outline of that pixel [48]. On one hand, every pixel of the HS picture contains a full otherworldly mark of length equivalent to the number of spectral groups of the HS cube. On the other hand, a dark scale



picture of the caught scene can be gotten utilizing any of the unearthly groups that show the spatial data gave by the picture sensor at a specific frequency [52][59].

Six individual arrangements of hyperspectral pictures were gotten for each liver sample, each arrangement consisting of a (5 cm × 6 cm) of the liver sample arrangement on a lined tray. Line-scan images were captured for exposure times of 6 msec at 3.12 nm intervals, and each set consisted of 600 line scans corresponding to 600 × 502 pixels per spectral band (3.6 sec for each cube image). The hyperspectral images were composed of a total of 128 spectral bands in the range from approximately 379 to 1050 nm, incorporated with a lens with range (400~1000 nm).

The drove Polychromatic light enlightens the liver tissue region of interest (ROI) and the camera target focal point gathers the radiation from the tissue and spectacles a picture on the passageway cut plane. The cut decides the field of imaging in spatial ways. The radiation from the cut is anticipated to the prism-grating; along these lines the bearing of the engendering of the radiation changes on its wavelength. The hyperspectral imaging framework comprises of an unearthly illuminator, which gives spectroscopic light to the example and a central plane exhibit locator, which catches the reflected spatial picture data, synchronized by a PC program.

#### 2.4 Image Preprocessing:

The preprocessing step predominantly incorporates de-noising and normalization. For thermal ablation recognition utilizing a hyperspectral imager, the noise is presented on account of the background. Moving average filter (K=10) is utilized to expel the noise impacts. Contour Mapping with designed K-mean clustering algorithm (K=8), next image clustering for the thermal region by variant threshold values to discriminate the distinct thermal regions, as explained in the block diagram in Figure 5.

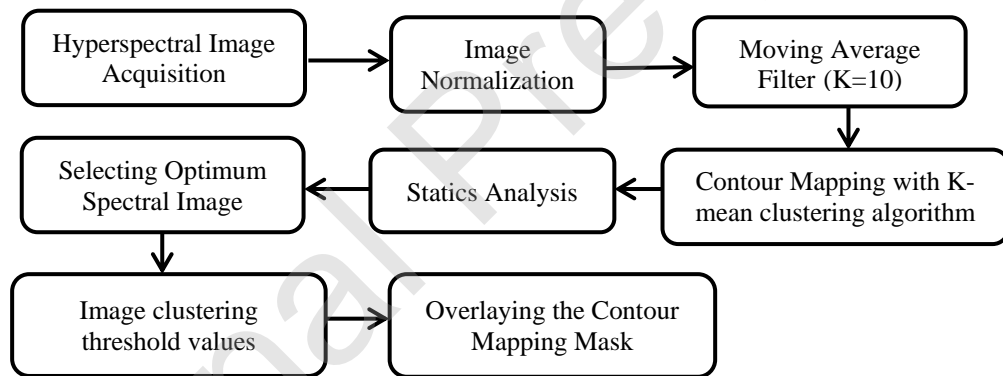


**Figure 1-** The Block Diagram of the Image Processing Algorithm sequence for the *ex-vivo* Bovine Liver Tissue Characterization

The issue with the spectral non-consistency of the light system and the impact of the dim current are wiped out through standardization of the picture information to discover the standardized Diffuse Reflectance of the sample. A standard reference whiteboard was set in the area of imaging and its information was used as the white reference [47,60]. This white reference is a standard Diffuse Reflectance that ought to be utilized for information standardization which shows the most extreme standard Diffuse Reflectance in every frequency and in catching time temperature. The Diffuse Reflectance from the board gives a gauge of the occurrence light on the organs at every frequency and standardizes the temperature changes, which is utilized in the standardization of the range. The dull current was caught by keeping the camera shade shut. At that point the information was standardized to locate a relative Diffuse Reflectance, as clarified in equation (1):

$$RF(\lambda) = \frac{R_{crude}(\lambda) - R_{black}(\lambda)}{R_{white}(\lambda) - R_{black}(\lambda)} \quad (1)$$

Where  $RF(\lambda)$  the determined relative Diffuse Reflectance esteem is for every Wavelength,  $R_{crude}(\lambda)$  is crude information brilliance estimation of a given pixel,  $R_{black}(\lambda)$  and  $R_{white}(\lambda)$

are, correspondingly, the dull current and the whiteboard brilliance obtained for each line and the otherworldly band of the sensor.

### 2.5 Spectral mapping and Acquisition:

The captured HSI cube is analyzed upon the 128 frames regarding the spectral range to select the optimum contrast wavelength, after The selective image at wavelength  $720 \pm 18.92$  nm have been normalized, then applying moving average filter ( $K=10$ ), afterward K-mean clustering up to 8-clusters for the contour display of the ablation and thermal regions and color mapping to the sample tissue, finally overlay of the images to produce the final algorithm for the thermal detection to the sample.

The caught data ought to be normalized to delight the spectral non-consistency of the enlightenment device. The raw information changes because of a few variables like light conditions, temperature, and non-uniform shape of the subject. To limit these changing conditions, otherworldly information must be normalized. The radiometric reflectance standardization process includes a pixel-to-pixel standardization of the hyperspectral image data to rate reflectance, as demonstrated in equation (2).

$$I_{new} = (I_{old} - \min_{old}) \frac{\max_{new} - \min_{new}}{\max_{old} - \min_{old}} + \min_{new} \quad (2)$$

Where, Normalization converts an n-dimensional grayscale old image  $I_{old}: \{A\}$  with intensity values in the range minimum ( $\min_{old}$ ) to maximum ( $\max_{old}$ ) into a new image  $I_{new}: \{A\}$  with intensity values in the range minimum ( $\min_{new}$ ) to maximum ( $\max_{new}$ ).

Applying the moving average filter, likewise well-known as arithmetic mean filter at ( $K=10$ ) for noise removal and image enhancement [61][62], as shown in equation (3).

$$f(x, y) = \frac{1}{hn} + \sum_{(k,L) \in W} \varphi(k, L) \quad (3)$$

Where ‘ $\varphi$ ’ is the noisy image,  $f(x, y)$  is the restored image, and ‘ $k$ ’ and ‘ $L$ ’ is the row and column coordinates respectively, within a window ‘ $W$ ’ of size ‘ $h \times n$ ’ where the operation takes place.

Next, applying the K-mean clustering (KMC) up to 8-clusters with variable threshold value from 0.2 up to 0.9 for variable thermal display, k-means is one of the least difficult unsupervised learning algorithms that take care of the clustering problem. We can formulate a general equation for the clustering algorithm; we can define the center-based clustering. Where variables define as  $N = \{n_1 \dots n_j\}$  is the set of ( $\hat{n}$ ) data points to be clustered in the d-dimensional,  $S = \{s_1 \dots s_j\}$  is the set of ( $K$ ) center points in the d-dimensional. The membership function  $M(s_j | n_i)$  describes the proportion of the data set  $n_i$  that related to the centroid  $s_j$  with limitation  $M(s_j | n_i) \geq 0$  and  $\sum_j^K M(s_j | n_i) = 1$ . A weight function  $\hat{w} = (n_i)$  demonstrated how much effects data set ( $n_i$ ) in recalculation the new center with limitation  $\hat{w} = (n_i) \geq 0$ .

We can define the general model for the center-based clustering steps, as follows:

1. Start the algorithm with deduced centers ( $S$ ).
2. For each number point ( $n_i$ ), compute its membership  $M(s_j | n_i)$  in each center ( $s_j$ ) and its weight  $\hat{w} = (n_i)$ .
3. For each center ( $s_j$ ), recalculate its position from all data points ( $n_i$ ) according to their membership and weight.

$$s_j = \frac{\sum_{i=1}^{\hat{n}} M(s_j | n_i) \hat{w} = (n_i) n_i}{\sum_{i=1}^{\hat{n}} M(s_j | n_i) \hat{w} = (n_i)} \quad (4)$$

4. Repeat step#2 and step#3 until merging.

K-mean clustering (KMC) algorithm improves is:

$$KMC(N, S) = \sum_{i=1}^n \min_{j \in \{1 \dots K\}} \|n_i - s_j\|^2 \quad (5)$$

This demonstrable function in equation (5) provides an algorithm which reduces the within-cluster variance.

$$(x + a)^n = \sum_{k=0}^n \binom{n}{k} x^k a^{n-k} \quad (6)$$

The weight and membership functions concerning *KMC* are:

$$M(s_j | n_i) = \begin{cases} 1 & \text{if } x = \arg \min_j \|n_i - s_j\|^2 \\ 0 & \text{otherwise} \end{cases} \quad (7)$$

$$w_{KMC}(n_i) = 1 \quad (8)$$

Finally, the contour image was overlaid on the selective spectral images. Regarding, the hyperspectral image justifications, each point in the liver tissue has a succession of relative Diffuse Reflectance in various wavelengths that makes the spectrum outline or unearthly mark of a point. The Diffuse Reflectance spectra of the pixels made out of thermal and ablated zones of a liver tissue surface were separated and used to compute a normal Diffuse Reflectance range. The degree of the thermal effect was divided into three levels (ablated, thermal influenced, and typical tissues), where these spectrum outlines have been assessed to discover a distinction between them in the tissue.

### 3. Results:

Capturing the images with the Hyperspectral camera and processing the image before and after thermal ablation. Image normalization, moving average filter and K-mean clustering were utilized as channels to upgrade the thermal and ablated district in images caught with the hyperspectral camera. The capturing time for each image is about 5~12 sec and calculation time is < 20-sec using DADiSP/SE software (DSP Development Corporation, 6.7 NI student edition B02, 2017) on a computer with processor Intel core i7 @1.8GHz with a 16 GB RAM. A conventional philosophy for target the identification and execution assessment was applied. The edges were balanced so as to expand the ablated recognition to guarantee identification of all the thermal /ablated districts. The exhibition was assessed utilizing the nature of discovery regarding the pathology.

After ablation, each sample was captured with the Hyperspectral camera, CCD microscopic camera (500X), and the thermal camera respectively thru several positions and at the same time for data recording purposes. Next, the liver sample was scanned at 1200 dpi to produce a high-resolution image to be used in image processing. Consequently, splitting it from the point of thermal ablation to explore more overall information about ablation and affected lateral cells to compare it with the captured Hyperspectral data. Thermal ablation continuously captured by a thermal camera for temperature monitoring, as shown in Figure 6.

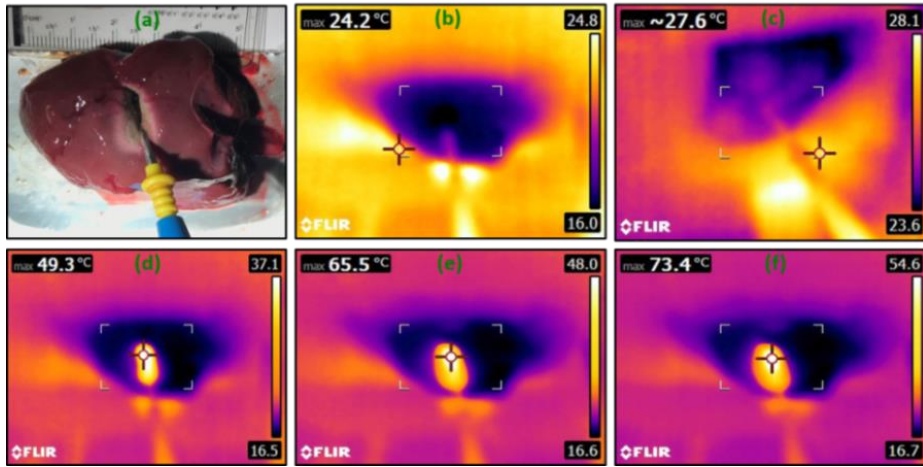


**Figure 6** - The RGB image for liver tissue during thermal ablation captured by CCD camera; (a) Thermal image before ablation captured by thermal camera; (b) Thermal image after 2 Sec ablation at 27.6° C captured by thermal camera; (c) Thermal image after 3 Sec ablation at 49.3° C captured by thermal camera; (d) Thermal image after 4 Sec ablation at 49.3° C captured by thermal camera; (e) Thermal image after 5 Sec ablation at 65.5° C captured by thermal camera ; (f) Thermal image after 6 Sec ablation at 73.4° C captured by thermal camera.

The imaging method utilized with this camera is a pushbroom scanner; the cut passageway restricts the imaging field. By moving the camera between consequent pictures, inevitably all locales and wavelengths of the item are caught [52]. By reproducing the resulting pictures, a monochromatic unearthly picture for every wavelength can be developed, demonstrating the role of the wavelength to Spectacles or conceal specific information.

The deliberate optical spectra of biological tissues from 400 to 1000 nm spread the noticeable and can be separated at the atomic level, which extraordinarily adds to the Diffuse Reflectance esteems estimated in specific reaches. The test was performed utilizing the *ex-vivo* bovine liver tissue, where captured HSI is scanned and segmented, selecting specific points to measure the diffuse reflectance of the ablation region and two different positions around it for measuring the thermal effect with respect to the normal tissue, as illustrated in Figure 7-a.

These signals were drawn in the graph illustrating the unique spectral signatures for each pixel point before normalization and moving average filter of the normal, ablated and thermal regions, as demonstrated in Figure 7-b. The spectral Diffuse Reflectance between the normal signal (Green solid line) and the ablation region (Blue solid line) is more identified in wavelength  $\geq 600 \pm 7.18$  nm. However, to identify between the normal (Green solid line) and thermally affected tissue (Brown and Red solid line) it was more recognized in wavelength  $\geq 500 \pm 6.24$  nm.

The bar chart for the spectral diffuse reflectance for each specific pixel point before normalization over the selective wavelengths ( $420 \pm 2.07$ ,  $520 \pm 6.24$ ,  $620 \pm 7.18$ ,  $720 \pm 18.92$ ,  $820 \pm 18.56$  and  $920 \pm 11.75$  nm), is illustrated in Figure 7-c.

we had used these spectral signatures as a guide for selecting the optimum spectral images which can be discriminate between the Four regions (Normal, Thermal#1, Thermal#2 and Ablation), to reduce the time of image processing for 128 frames to be only six spectral images starting from  $420 \pm 2.07$  nm up to  $920 \pm 11.75$  nm, as shown in Figure 7.

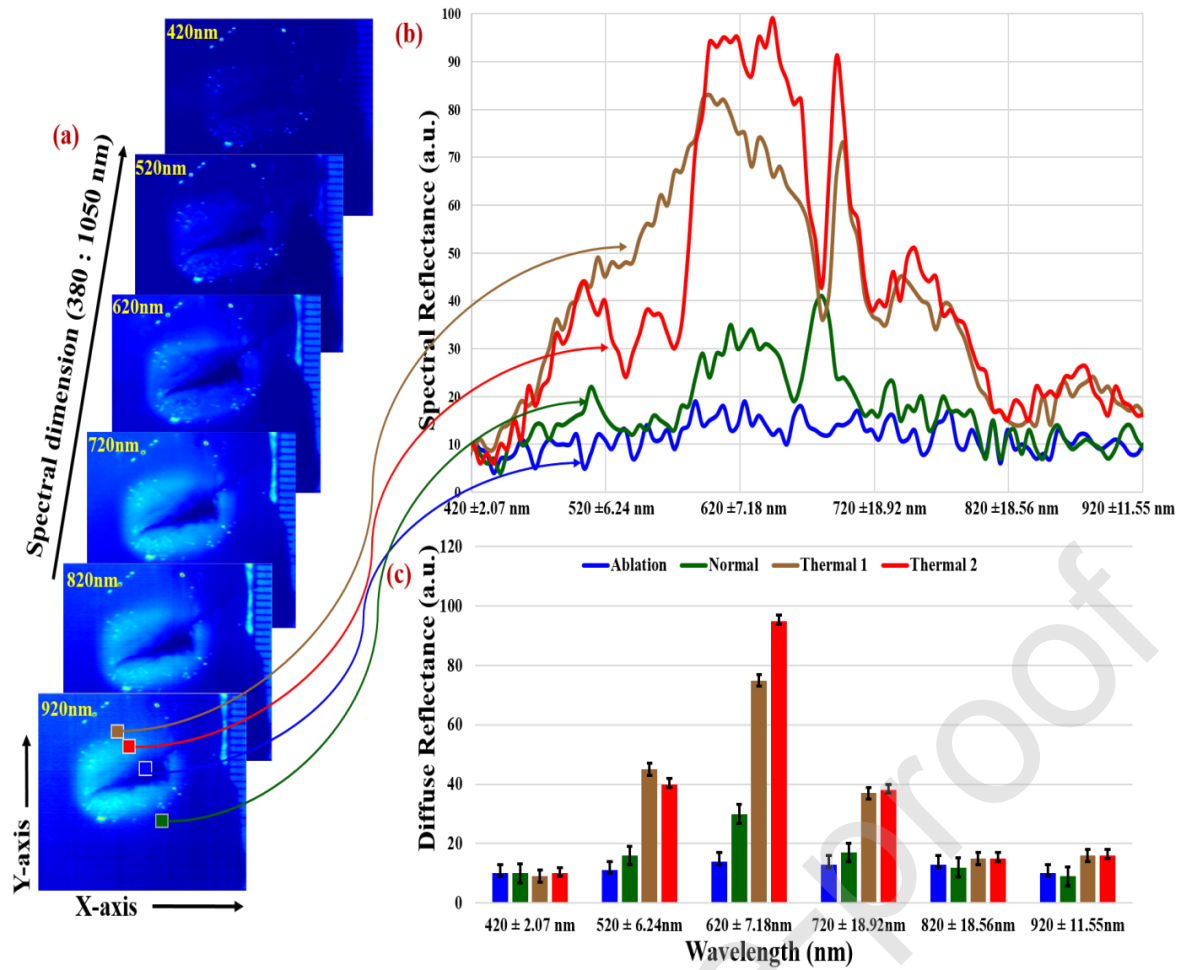


**Figure 7** - Hyperspectral image Signal Signature for pixel intensity of Liver Tissue ; (a) The Hyperspectral image segmentation captured in both the visible and Near IR range;(b) The Spectral Diffuse reflectance for selective specific pixel point before normalization,where the blue pixel for demonstrate the Diffuse Reflectance of the Ablation region where its presented in the gragph by the blue solid line;the Green pixel is diffuse the Diffuse Reflectance of the Normal not affected with thermal region in the liver tissue where its presented in the gragph by the green solid line,additionally the thermal#1 and thermal#2 regions are represented by red and brown pixel and solid lines repsectively;(c) The Bar Chart for The Spectral Diffuse reflectance for each specific pixel point before normalization over the Selective Wavelengths (420±2.07 ,520±6.24 ,620±7.18 ,720±18.92 ,820±18.56 and 920±11.75 nm).

The acquiring spectral images from the hyperspectral camera of the *ex-vivo* bovine liver sample after ablation and image processing utilizing our custom algorithm (Normalization and Moving average  $K=10$  ) at (420±2.07 ,520±6.24 ,620±7.18 ,720±18.92 ,820±18.56 and 920±11.75 nm) , as illustrated in Figure 8-a,b,c,d,e,f respectively. The color bar for each spectral image mapping the Diffuse Reflectance intensity for each point in these images, where the ablation and the normal tissue having various values. The vertical red dashed line (Column line) was selected to give information from different regions (Normal, , Thermal#1, Thermal#2 and Ablated).



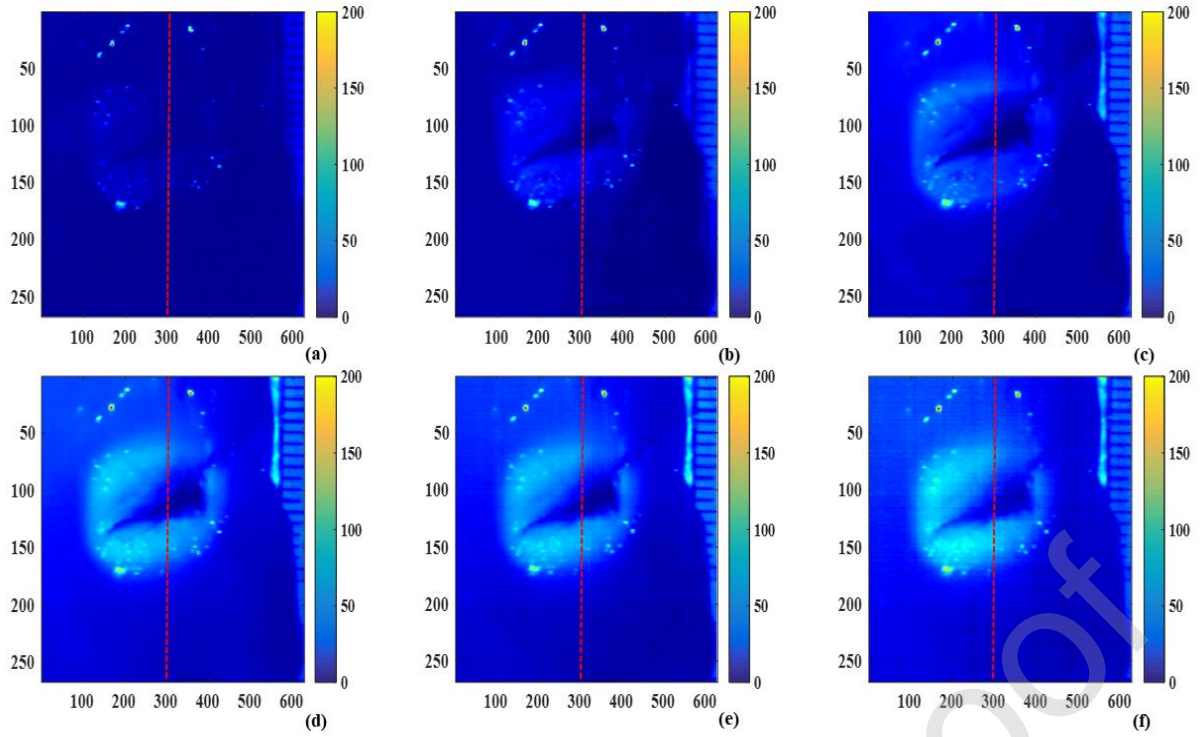


**Figure 8** - The *ex-vivo* Bovine Liver Sample after Ablation and image processing utilizing our Custom Algorithm (Normalization, Moving average  $K=10$ ) at Spectral Images ( $420\pm 2.07$ ,  $520\pm 6.24$ ,  $620\pm 7.18$ ,  $720\pm 18.92$ ,  $820\pm 18.56$  and  $920\pm 11.75$  nm). The vertical red dashed line (Column line at 300 x-axis) was selected to give information from different regions (Normal, Thermal#1, Thermal#2 and Ablated).

The calculated contour mapping of the selective spectral images in Figure 8 is represented in Figure 9. Where No difference could be noticed at wavelength  $420\pm 2.07$  nm between the Normal versus thermal region as well the Normal versus ablation region. While at wavelength  $520\pm 6.24$  nm we could differentiate between normal and thermal regions but we couldn't differentiate between normal and ablated regions. At wavelength 620 nm we could better differentiate between normal and thermal regions and we could barely differentiate between normal and ablated regions. Starting from wavelength range 720~920 nm we could distinguish between the four regions but the optimum wavelength was  $720\pm 18.92$  nm as it had a higher signal to noise ratio compared to wavelengths  $820\pm 18.56$  nm and  $920\pm 11.75$  nm respectively which had higher noise interaction.

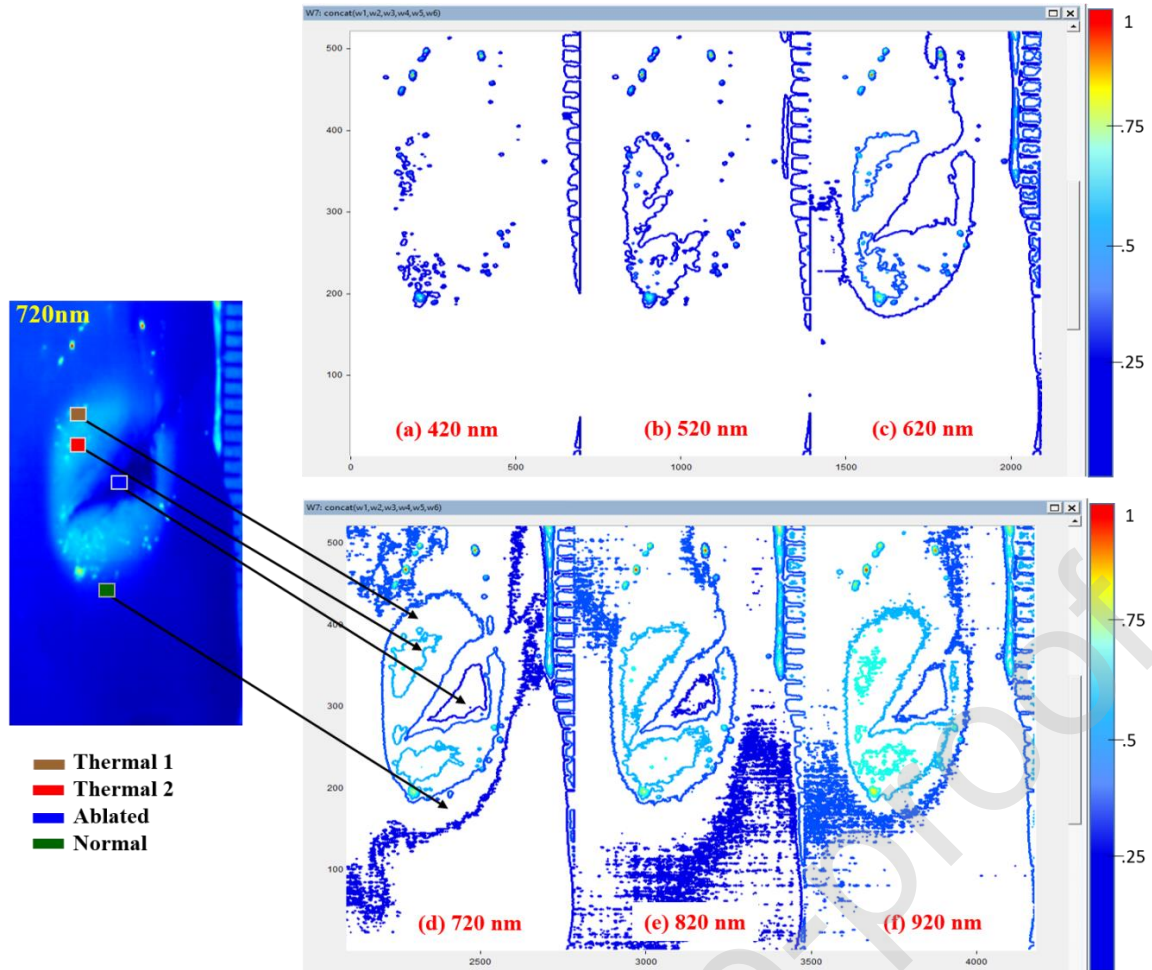


**Figure 9** – Contour Mapping to discriminate between the Four regions (Normal, Thermal#1, Thermal#2 and Ablation) of the Spectral Images with standard deviation( $\delta$ ) from left to right ( $420 \pm 2.07$ ,  $520 \pm 6.24$ ,  $620 \pm 7.18$ ,  $720 \pm 18.92$ ,  $820 \pm 18.56$  and  $920 \pm 11.75$  nm), respectively.

To determine the optimum wavelength range and validate the contour mapping in Figure 9 we have to discriminate between the Four regions (Normal, Thermal#1, Thermal#1, and Ablation) by statistically calculating the Diffuse Reflectance intensity of the vertical red dashed line at (300 x-axes) in all the spectral images ( $420 \pm 2.07$ ,  $520 \pm 6.24$ ,  $620 \pm 7.18$ ,  $720 \pm 18.92$ ,  $820 \pm 18.56$  and  $920 \pm 11.75$  nm), from Figure 8. Where, the bar chart for the Diffuse Reflectance Intensity of the *ex-vivo* Liver Sample images after normalization and Moving average filter over The Selective Wavelengths ( $420 \pm 2.07$ ,  $520 \pm 6.24$ ,  $620 \pm 7.18$ ,  $720 \pm 18.92$ ,  $820 \pm 18.56$  and  $920 \pm 11.75$  nm) at column line at (300 x-axis), as displayed in Figure 10-a.

The Diffuse Reflectance intensity of the normal tissue (green color bar) and the ablated region (blue color bar) was almost the same value at wavelength  $420 \pm 2.07$  nm (9 a.u) and at wavelength  $520 \pm 6.24$  nm (5 a.u). However, there was variation between the normal and the thermal regions starting from wavelength  $520 \pm 6.24$  nm (Normal = 5 a.u, Thermal#1= 18 a.u, and Thermal#2= 20 a.u).

We noticed that the optimum wavelength to discriminate between the Four regions (Normal, Thermal#1, Thermal#1 and Ablation) at wavelength  $720 \pm 18.922$  nm. where, the Diffuse Reflectance intensity values (Normal = 23 a.u, Ablation = 8 a.u, Thermal#1= 42 a.u and Thermal#2= 55 a.u). Additionally, The Spatial Signature for column line at (300 x-axis) of the *ex-vivo* Liver Sample images after normalization and Moving average filter over The Selective Wavelengths ( $420 \pm 2.07$ ,  $520 \pm 6.24$ ,  $620 \pm 7.18$ ,  $720 \pm 18.92$ ,  $820 \pm 18.56$  and  $920 \pm 11.75$  nm) as displayed in Figure 10-b.

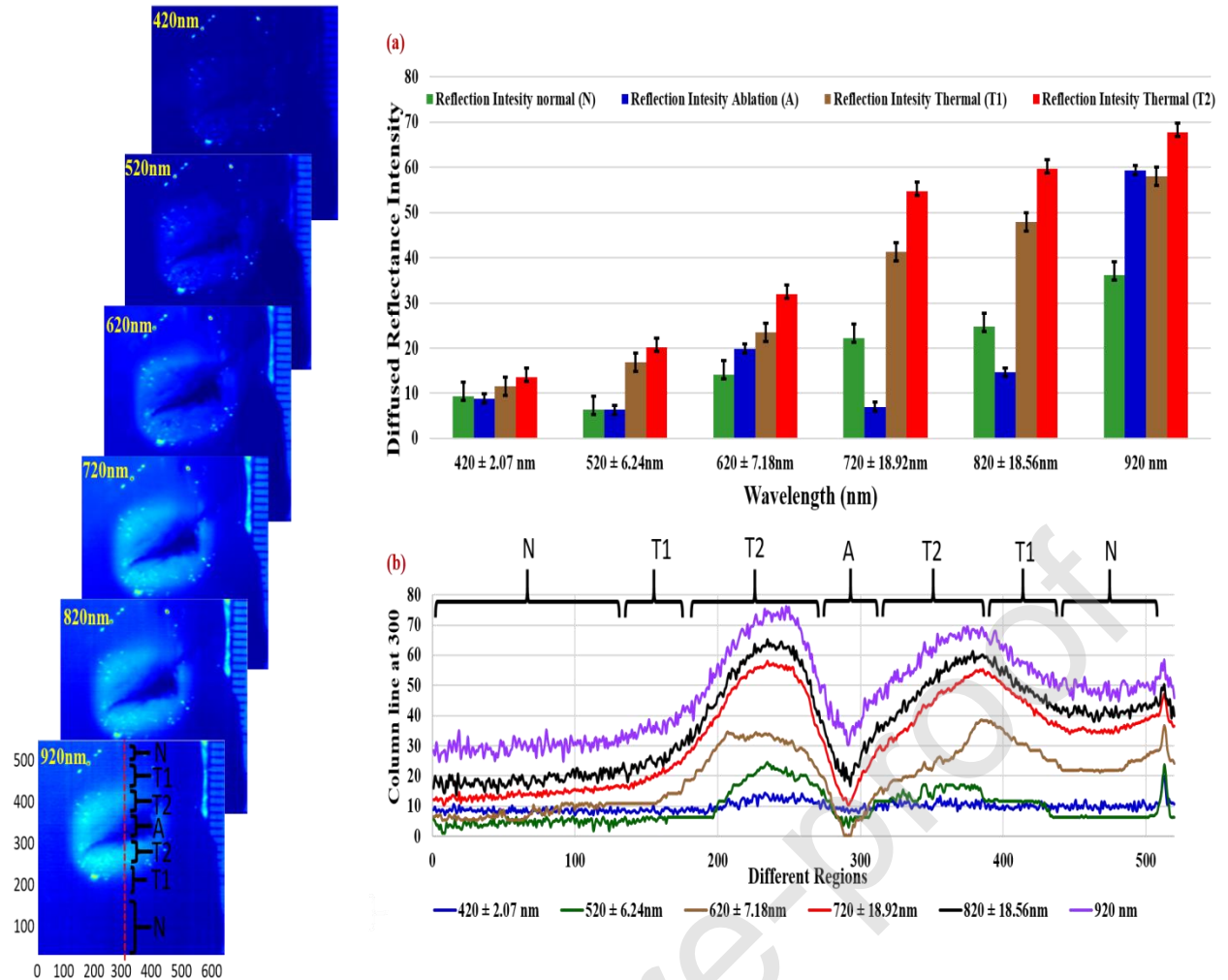


**Figure 10** – (a) The Bar Chart for the Diffuse Reflectance Intensity of the *ex-vivo* Liver Sample images after normalization and Moving average filter over The Selective Wavelengths ( $420 \pm 2.07$ ,  $520 \pm 6.24$ ,  $620 \pm 7.18$ ,  $720 \pm 18.92$ ,  $820 \pm 18.56$  and  $920 \pm 11.75$  nm) at column line at (300 x-axis); (b) The Spatial Signature for column line at (300 x-axis) of the *ex-vivo* Liver Sample images after normalization and Moving average filter over The Selective Wavelengths ( $420 \pm 2.07$ ,  $520 \pm 6.24$ ,  $620 \pm 7.18$ ,  $720 \pm 18.92$ ,  $820 \pm 18.56$  and  $920 \pm 11.75$  nm).

The calculated standard deviation ( $\delta$ ) for the selective wavelengths ( $420 \pm 2.07$ ,  $520 \pm 6.24$ ,  $620 \pm 7.18$ ,  $720 \pm 18.92$ ,  $820 \pm 18.56$  and  $920 \pm 11.75$  nm) and the Sample Variance ( $S^2$ ) for The Selective Wavelengths ( $420 \pm 4.28$ ,  $520 \pm 38.89$ ,  $620 \pm 51.59$ ,  $720 \pm 358.08$ ,  $820 \pm 344.40$  and  $920 \pm 138.07$  nm) of the *ex-vivo* Liver Sample.

It was clearly illustrated by the statistical calculation of the Diffuse Reflectance intensity that the optimum contrast between ablated, thermal influenced and normal tissues were the hyperspectral image at wavelength 720 nm ( $\delta = 18.9$ ,  $S^2 = 358.07$ ).

After selecting the optimum spectral image ( $720 \pm 358.08$  nm), the image was Normalized and the noise was removed by moving average filter ( $K=10$ ). Contour mapping with the K-mean image clustering ( $K=8$ ) at variable threshold value to reveal the different thermal effects and ablation zone in the sample. Finally, Overlaying the contour mapping according to the threshold value over the original HS image, as represented in Figure 11.

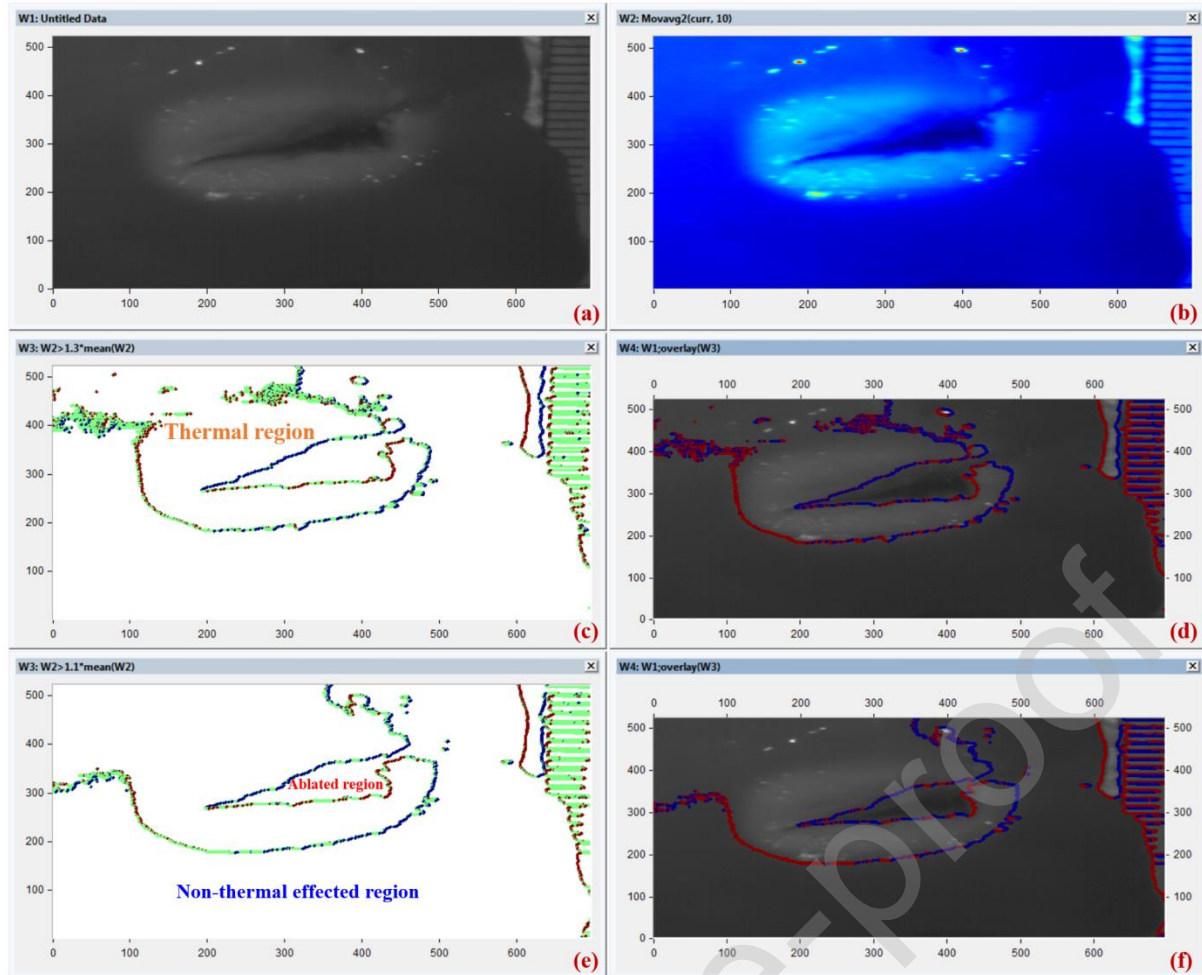


**Figure 11** - Image processing for captured HSI of *ex-vivo* bovine liver sample at wavelength  $720 \pm 358.08$  nm ; (a) Captured HSI at wavelength  $720 \pm 358.08$  nm ; (b) Image Normalization and Moving average filter (K=10) for noise removing ; (c) Contour mapping with the K-mean image clustering (K=8) at threshold value = 1.3 to reveal the whole thermal effect region in the sample;(d) Overlaying the contour mapping according to the threshold value over the original HSI to discriminate the thermal region ; (e) Contour mapping with the K-mean image clustering (K=8) at threshold value = 1.1 to reveal the the ablation and the normal region region in the sample;(f) Overlaying the contour mapping according to the threshold value over the original HSI to discriminate the Ablation / Normal (Non-thermal effect) region.

#### 4. Discussion:

Thermal ablation is the dominant modalities for ablative treatment of un-resection liver tumors, where monitoring the ablation process with the right image-guided inclusion of terminals is vital to accomplish a fruitful removal of tumors with minimum thermal damage of liver [38–40,63]. The removal procedure is routinely observed with computed tomography, or b-mode sonography to guarantee fruitful tumor removal with fitting wellbeing edges; however, tissue scarring or gas bubble development may hamper translation of sonographic pictures [27,28,37,63].

Recently, many researchers have developed several imaging methods to guarantee suitable removal of liver malignant and metastases utilizing non-intrusive or negligibly obtrusive systems with respect to the conventional excisional biopsy. Of these imaging techniques, the CT modality utilizing MWA on three *ex-vivo* porcine samples, the outcomes showed ablation diameter ( $4.1 \pm 0.2 \times 5.6 \pm 0.2$ ) [34]. Other study combine both the US and CT utilizing MWA on four *ex-vivo* calf livers, the results showed ablation diameter ( $2.1 \pm 0.1$ mm (15 markers used) [35]. A study using Contrast Enhanced Ultrasonography (CEUS) technique with ILTT on 12-patient clinical trial, the results present ablation diameter (11~16 mm) [36]. infrared thermography monitoring [37,38], real-time ultrasound elastography [39], high resolution US [39,40] and electrode vibration elastography [41].



Anyway, all checking modalities have their issues to give an exact proclamation about the achievement of the ablation. On the other side hyperspectral imaging (HSI) method provides specific wavelengths (spectral image) across the electromagnetic spectrum as it collects spatial and spectral information for the specimen under investigation [42,64], some of these techniques could be summarized, as presented in Table 1.

We measure the diffuse reflectance of the *ex-vivo* liver sample after ablation to discriminate between the ablation region and two other different positions around it for measuring the thermal effect with respect to the normal tissue, as illustrated in Figure 7-a. These signals were drawn in the graph illustrating the unique spectral signatures for each pixel point before normalization and moving average filter of the normal, ablated and thermal regions, as demonstrated in Figure 7-b. We had used these spectral signatures and the bar chart in Figure 7-c, as a guide for selecting the optimum spectral images which can be discriminate between the Four regions (Normal, Thermal#1, Thermal#2 and Ablation).

To decrease the time consuming for the image processing of the whole cube image of the *ex-vivo* bovine liver sample after ablation, we select the optimum spectral images ( $420 \pm 2.07$ ,  $520 \pm 6.24$ ,  $620 \pm 7.18$ ,  $720 \pm 18.92$ ,  $820 \pm 18.56$  and  $920 \pm 11.75$  nm) from the hyperspectral camera regarding the spectral signature from Figure 7-b, to compare between the contrast spectral images, as displayed in Figure 8.

Figure 9 represents the calculated contour mapping of the selective spectral images in Figure 8. Where, we couldn't discriminate between the ablated, thermal and normal regions at wavelength  $420 \pm 2.07$  nm. While at wavelength  $520 \pm 6.24$  nm we could differentiate between normal and thermal regions but we couldn't differentiate between normal and ablated regions. At wavelength 620 nm we could better differentiate between normal and thermal regions and we could barely differentiate between normal and ablated regions. Starting from wavelength range 720~920 nm we could distinguish between the four regions but the optimum wavelength was  $720 \pm 18.92$  nm as it had a higher signal to noise ratio compared to wavelengths  $820 \pm 18.56$  nm and  $920 \pm 11.75$  nm respectively which had higher noise interaction.

To determine the optimum wavelength range and validate the contour mapping in Figure 9 we have to discriminate between the Four regions (Normal, Thermal#1, Thermal#1, and Ablation) by statistically calculating the Diffuse Reflectance intensity of the vertical red dashed line at (300 x-axes) in all the spectral images ( $420 \pm 2.07$ ,  $520 \pm 6.24$ ,  $620 \pm 7.18$ ,  $720 \pm 18.92$ ,  $820 \pm 18.56$  and  $920 \pm 11.75$  nm), from Figure 8. Where, the bar chart for the Diffuse Reflectance Intensity of the *ex-vivo* Liver Sample images after normalization and Moving average filter over The Selective Wavelengths ( $420 \pm 2.07$ ,  $520 \pm 6.24$ ,  $620 \pm 7.18$ ,  $720 \pm 18.92$ ,  $820 \pm 18.56$  and  $920 \pm 11.75$  nm) at column line at (300 x-axis), as displayed in Figure 10-a.

We noticed that the optimum wavelength to discriminate between the Four regions (Normal, Thermal#1, Thermal#1 and Ablation) at wavelength  $720 \pm 18.92$  nm. where, the Diffuse Reflectance intensity values (Normal = 23 a.u., Ablation = 8 a.u., Thermal#1 = 42 a.u. and Thermal#2 = 55 a.u.). Additionally, The Spatial Signature for column line at (300 x-axis) of the *ex-vivo* Liver Sample images after normalization and Moving average filter over The Selective Wavelengths ( $420 \pm 2.07$ ,  $520 \pm 6.24$ ,  $620 \pm 7.18$ ,  $720 \pm 18.92$ ,  $820 \pm 18.56$  and  $920 \pm 11.75$  nm) as displayed in Figure 10-b.

The work introduced in this paper with the objective of building up a custom optical imaging system and associated K-mean clustering algorithm to characterize and evaluate different thermal effects of the investigated *ex-vivo* beef liver sample before and after Radiofrequency ablation (RFA). The results demonstrated that the optimum wavelength range (620~920 nm)



differentiated between the normal region, thermal, and ablated regions of the investigated samples, as displayed in Figure 8. However, the optimum wavelength was  $720 \pm 18.92$  nm and as it had a higher signal to noise ratio compared to wavelengths  $820 \pm 18.56$  nm and  $920 \pm 11.75$  nm respectively which had higher noise interaction.

Hyperspectral imaging is a powerful tool in monitoring the thermal ablation with minimum time, but it is very expensive regarding the commercial CCD camera and it can't work in real-time as the spectral cube need to be analyzed for the 128 frames and consume more time for image processing, and to avoid that topic we had to discriminate the optimum wavelength ( $720 \pm 18.92$  nm), which decrease the time consuming and provide precise information to demonstrate significant monitoring of the ablation process to accomplish a fruitful ablation of tumors with minimum thermal damage of liver. Our study was limited by *ex-vivo* liver tissue utilizing HS camera; further investigations will be carried out in the future work for validation using commercial CCD camera attached with the optical filter ( $720 \pm 18.92$ ) and several types of tissues with different properties.

#### *Declarations*

The authors declare no conflict of interest and Stated that they have no competing interest. There are No funders and No one had any role in the design of the study; in the collection, analyses, or interpretation of data; in the writing of the manuscript, or in the decision to publish the results .This research did not receive any specific grant from funding agencies in the public, commercial, or not-for-profit sectors.

#### **Author Contributions:**

**Conceptualization:** Mohamed Hisham Aref, Ibrahim H. Aboughaleb, and Yasser H. El-Sharkawy.

**Formal analysis:** Mohamed Hisham Aref, Ibrahim H. Aboughaleb

**Investigation:** Mohamed Hisham Aref, Ibrahim H. Aboughaleb

**Methodology:** Mohamed Hisham Aref, Ibrahim H. Aboughaleb, and Yasser H. El-Sharkawy

**Resources:** Mohamed Hisham Aref, Ibrahim H. Aboughaleb

**Image Algorithm:** Yasser H. El-Sharkawy

**Supervision:** Yasser H. El-Sharkawy

**Writing – original draft:** Mohamed Hisham Aref, Ibrahim H. Aboughaleb

**Writing – review & editing:** Mohamed Hisham Aref, Ibrahim H. Aboughaleb, and Yasser H. El-Sharkawy

#### **References**

- [1] S.J. Yu, A concise review of updated guidelines regarding the management of hepatocellular carcinoma around the world: 2010-2016, Clin. Mol. Hepatol. 22 (2016) 7–17. <https://doi.org/10.3350/cmh.2016.22.1.7>.
- [2] J. Ferlay, I. Soerjomataram, R. Dikshit, S. Eser, C. Mathers, M. Rebelo, D.M. Parkin, D. Forman, F. Bray, Cancer incidence and mortality worldwide: sources, methods and major patterns in GLOBOCAN 2012, Int. J. Cancer. 136 (2015) E359–E386.
- [3] L. Mobarak, M.M. Nabeel, W. El Agawy, RISK FACTORS OF HEPATOCELLULAR CARCINOMA IN EGYPTIAN PATIENTS WITH CHRONIC LIVER DISEASE, AL-AZHAR ASSIUT Med. J. 13 (2015).
- [4] A.S. Ibrahim, H.M. Khaled, N.N. Mikhail, H. Baraka, H. Kamel, Cancer incidence in Egypt: Results of the national population-based cancer registry program, J. Cancer Epidemiol. 2014 (2014). <https://doi.org/10.1155/2014/437971>.
- [5] K.M. Kim, D.H. Sinn, S. Jung, G. Gwak, Y. Paik, M.S. Choi, The recommended treatment algorithms of the BCLC and HKLC staging systems : does following these always improve survival rates for HCC patients ?, (2016) 1490–1497. <https://doi.org/10.1111/liv.13107>.
- [6] T. Longerich, K. Breuhahn, P. Schirmacher, Molecular pathology of liver tumors, 2013. [https://doi.org/10.1007/978-1-4614-4900-3\\_3](https://doi.org/10.1007/978-1-4614-4900-3_3).
- [7] W.M. Rashed, M.A.M. Kandeil, M.O. Mahmoud, S. Ezzat, Hepatocellular Carcinoma (HCC) in Egypt: A comprehensive overview, J. Egypt. Natl. Canc. Inst. 32 (2020) 1–11.
- [8] M.J. Englesbe, S.P. Patel, K. He, R.J. Lynch, D.E. Schaubel, C. Harbaugh, S.A. Holcombe, S.C. Wang, D.L. Segev, C.J. Sonnenday, Sarcopenia and mortality after liver transplantation, J. Am. Coll. Surg. 211 (2010) 271–278.
- [9] A. Forner, M. Gilibert, J. Bruix, J.L. Raoul, Treatment of intermediate-stage hepatocellular carcinoma,

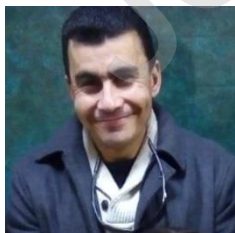
- Nat. Rev. Clin. Oncol. 11 (2014) 525–535. <https://doi.org/10.1038/nrclinonc.2014.122>.
- [10] J. Bruix, M. Reig, M. Sherman, Evidence-based diagnosis, staging, and treatment of patients with hepatocellular carcinoma, *Gastroenterology*. 150 (2016) 835–853.
  - [11] E.J.A. Morris, D. Forman, J.D. Thomas, P. Quirke, E.F. Taylor, L. Fairley, B. Cottier, G. Poston, Surgical management and outcomes of colorectal cancer liver metastases, *Br. J. Surg.* 97 (2010) 1110–1118.
  - [12] C.E. Tatsui, R.J. Stafford, J. Li, J.N. Sellin, B. Amini, G. Rao, D. Suki, A.J. Ghia, P. Brown, S. Lee, C.E. Cowles, J.S. Weinberg, L.D. Rhines, surgery in the management of spinal metastasis, 23 (2015) 400–411. <https://doi.org/10.3171/2015.3.SPINE15210.Submitted>.
  - [13] T. Livraghi, H. Mäkisalo, P. Line, Treatment options in hepatocellular carcinoma today Stage 0 Stage A-C, (2011) 22–29. <https://doi.org/10.1177/145749691110000105>.
  - [14] C.L. Brace, Microwave tissue ablation: Biophysics, technology, and applications, *Crit. Rev. Biomed. Eng.* 38 (2010) 65–78. <https://doi.org/10.1615/CritRevBiomedEng.v38.i1.60>.
  - [15] B. Imene, B. Farid, B. Khaoula, CT-guided microwave liver tumors ablation and automatic adjustment of frequency, 2 (2018).
  - [16] W.A. N'Djin, B. Gerold, J. Vion-Bailly, M.S. Canney, A. Nguyen-Dinh, A. Carpentier, J.-Y. Chapelon, Capacitive micromachined ultrasound transducers for interstitial high-intensity ultrasound therapies, *IEEE Trans. Ultrason. Ferroelectr. Freq. Control.* 64 (2017) 1245–1260.
  - [17] J. Macdonell, N. Patel, S. Rubino, G. Ghoshal, G. Fischer, E.C. Burdette, R. Hwang, J.G. Pilitsis, Magnetic resonance-guided interstitial high-intensity focused ultrasound for brain tumor ablation, 44 (2018) 1–6. <https://doi.org/10.3171/2017.11.FOCUS17613>.
  - [18] T.R. Fosnight, F.M. Hooi, R.D. Keil, A.P. Ross, S. Subramanian, T.G. Akinyi, J.K. Killin, P.G. Barthe, S.M. Rudich, S.A. Ahmad, Echo decorrelation imaging of rabbit liver and VX2 tumor during in vivo ultrasound ablation, *Ultrasound Med. Biol.* 43 (2017) 176–186.
  - [19] H. Zhi-Yu, L. Ping, Y. Xiao-Ling, C. Zhi-Gang, L. Fang-Yi, Y. Jie, A clinical study of thermal monitoring techniques of ultrasound-guided microwave ablation for hepatocellular carcinoma in high-risk locations, *Sci. Rep.* 7 (2017) 1–8. <https://doi.org/10.1038/srep41246>.
  - [20] Local recurrence after laparoscopic radiofrequency ablation of malignant liver tumors : Results of a contemporary series, (2017) 830–834. <https://doi.org/10.1002/jso.24599>.
  - [21] T.J. Vogl, A. Dommermuth, B. Heinle, N.-E.A. Nour-Eldin, T. Lehnert, K. Eichler, S. Zangos, W.O. Bechstein, N.N.N. Naguib, Colorectal Cancer Liver Metastases: Long-Term Survival and Progression-Free Survival After Thermal Ablation Using Magnetic Resonance-Guided Laser-Induced Interstitial Thermotherapy in 594 Patients Analysis of Prognostic Factors, *Invest. Radiol.* 49 (2014) 48–56.
  - [22] R. Jafari, H. Almqvist, H. Axelsson, M. Ignatushchenko, T. Lundbäck, P. Nordlund, D.M. Molina, The cellular thermal shift assay for evaluating drug target interactions in cells, (2014). <https://doi.org/10.1038/nprot.2014.138>.
  - [23] A.M. James, Thermal and energetic studies of cellular biological systems, Butterworth-Heinemann, 2016.
  - [24] K.H. Kim, Y.S. Yoon, C.S. Yu, T.W. Kim, H.J. Kim, P.N. Kim, H.K. Ha, J.C. Kim, Comparative analysis of radiofrequency ablation and surgical resection for colorectal liver metastases, *J. Korean Surg. Soc.* 81 (2011) 25–34.
  - [25] W. Yang, K. Yan, S.N. Goldberg, M. Ahmed, J.-C. Lee, W. Wu, Z.-Y. Zhang, S. Wang, M.-H. Chen, Ten-year survival of hepatocellular carcinoma patients undergoing radiofrequency ablation as a first-line treatment, *World J. Gastroenterol.* 22 (2016) 2993.
  - [26] M. Ahmed, S.N. Goldberg, Basic science research in thermal ablation, *Surg. Oncol. Clin.* 20 (2011) 237–258.
  - [27] B.M. Künzli, P. Abitabile, C.A. Maurer, Radiofrequency ablation of liver tumors: actual limitations and potential solutions in the future, *World J. Hepatol.* 3 (2011) 8.
  - [28] Y.K. Cho, H. Rhim, S. Noh, Radiofrequency ablation versus surgical resection as primary treatment of hepatocellular carcinoma meeting the Milan criteria: a systematic review, *J. Gastroenterol. Hepatol.* 26 (2011) 1354–1360.
  - [29] P. Dvorak, P. Hoffmann, M. Brodak, J. Kosina, J. Pacovsky, J. Raupach, A. Krajina, Percutaneous radiofrequency and microwave ablation in the treatment of renal tumors – 10 years of experience, *Wideochirurgia I Inne Tech. Maloinwazyjne.* 12 (2017) 394–402. <https://doi.org/10.5114/wiitm.2017.72322>.
  - [30] T. Livraghi, F. Meloni, L. Solbiati, G. Zanus, C.I.G. using A. system, Complications of microwave ablation for liver tumors: results of a multicenter study, *Cardiovasc. Intervent. Radiol.* 35 (2012) 868–874.
  - [31] H.X. Xu, M. De Lu, Technology and Method 窑 Percutaneous ultrasound - guided thermal ablation for liver tumor with artificial pleural effusion or ascites Methods : Results : Conclusions :, 29 (2010).
  - [32] D.S.K. Lu, S.S. Raman, P. Limanond, D. Aziz, J. Economou, R. Busuttil, J. Sayre, Influence of large peritumoral vessels on outcome of radiofrequency ablation of liver tumors, *J. Vasc. Interv. Radiol.* 14 (2003) 1267–1274.
  - [33] H. Takahashi, M. Akyuz, E. Aksoy, K. Karabulut, E. Berber, Local recurrence after laparoscopic radiofrequency ablation of malignant liver tumors: Results of a contemporary series, *J. Surg. Oncol.* 115

- (2017) 830–834.
- [34] J. Paul, T.J. Vogl, A. Chacko, Dual energy computed tomography thermometry during hepatic microwave ablation in an ex-vivo porcine model, *Phys. Medica*. 31 (2015) 683–691.
  - [35] X. Yu, F. Liu, P. Liang, A.D. Era, Z. Cheng, Z. Han, Microwave ablation assisted by a computerised tomography–ultrasonography fusion imaging system for liver lesions: An ex vivo experimental study, *Int. J. Hyperth.* 27 (2011) 172–179.
  - [36] M. Atri, M.R. Gertner, M.A. Haider, R.A. Weersink, J. Trachtenberg, Contrast-enhanced ultrasonography for real-time monitoring of interstitial laser thermal therapy in the focal treatment of prostate cancer, *Can. Urol. Assoc. J.* 3 (2009) 125.
  - [37] F. Primavesi, S. Swierczynski, E. Klieser, T. Kiesslich, T. Jäger, R. Urbas, J. Hutter, D. Neureiter, D. Öfner, S. Stättner, Thermographic real-time-monitoring of surgical radiofrequency and microwave ablation in a perfused porcine liver model, *Oncol. Lett.* 15 (2018) 2913–2920. <https://doi.org/10.3892/ol.2017.7634>.
  - [38] S. Swierczynski, F. Primavesi, E. Klieser, T. Kiesslich, T. Jäger, R. Illig, D. Neureiter, D. Ofner, S. Stättner, 382. Thermographic monitoring of radiofrequency and microwave ablation in a perfused porcine liver model, *Eur. J. Surg. Oncol.* 40 (2014) S147. <https://doi.org/10.1016/j.ejso.2014.08.372>.
  - [39] Y.Z. Zhang, T. Xu, H.Y. Gong, C.Y. Li, X.H. Ye, H.J. Lin, M.P. Shen, Y. Duan, T. Yang, X.H. Wu, Application of high-resolution ultrasound, real-time elastography, and contrast-enhanced ultrasound in differentiating solid thyroid nodules, *Med. (United States)*. 95 (2016). <https://doi.org/10.1097/MD.0000000000005329>.
  - [40] P. Wiggermann, K. Brunn, J. Rennert, M. Loss, H. Wobser, A.G. Schreyer, C. Stroszczynski, E.M. Jung, Monitoring during hepatic radiofrequency ablation (RFA): Comparison of real-time ultrasound elastography (RTE) and contrast-enhanced ultrasound (CEUS): First clinical results of 25 patients, *Ultraschall Der Medizin-European J. Ultrasound*. 34 (2013) 590–594.
  - [41] R.J. Dewall, T. Varghese, C.L. Brace, Visualizing ex vivo radiofrequency and microwave ablation zones using electrode vibration elastography, *Med. Phys.* 39 (2012) 6692–6700. <https://doi.org/10.1118/1.4758061>.
  - [42] T. Henedige, S.K. Venkatesh, Imaging of hepatocellular carcinoma: diagnosis, staging and treatment monitoring, *Cancer Imaging*. 12 (2012) 530.
  - [43] A. Robles-Kelly, C.P. Huynh, Imaging Spectroscopy for Scene Analysis, *Imaging Spectrosc. Scene Anal.* (2013). <https://doi.org/10.1007/978-1-4471-4652-0>.
  - [44] J.M. Bioucas-Dias, A. Plaza, G. Camps-Valls, P. Scheunders, N. Nasrabadi, J. Chanussot, Hyperspectral remote sensing data analysis and future challenges, *IEEE Geosci. Remote Sens. Mag.* 1 (2013) 6–36.
  - [45] Q. Li, X. He, Y. Wang, H. Liu, D. Xu, F. Guo, Review of spectral imaging technology in biomedical engineering: achievements and challenges, *J. Biomed. Opt.* 18 (2013) 100901.
  - [46] H. Akbari, L. Halig, D.M. Schuster, B. Fei, A. Osunkoya, V. Master, P. Nieh, G. Chen, Hyperspectral imaging and quantitative analysis for prostate cancer detection, *J. Biomed. Opt.* 17 (2012) 76005.
  - [47] L. Gao, R.T. Smith, Optical hyperspectral imaging in microscopy and spectroscopy—a review of data acquisition, *J. Biophotonics*. 8 (2015) 441–456.
  - [48] T. Delineation, H. Fabelo, S. Ortega, R.L. Id, D.M. Id, G.M. Callic, E. Ju, D. Bulters, H.B. Id, A. Szolna, J.F. Piñeiro, C. Sosa, A.J.O. Shanahan, S. Bisshopp, D. Ravi, B.R. Kiran, A. Vega, B. Abelardo, G. Yang, B. Stanciulescu, An Intraoperative Visualization System Using Hyperspectral Imaging to Aid in Brain, (2018). <https://doi.org/10.3390/s18020430>.
  - [49] H. Akbari, K. Uto, Y. Kosugi, K. Kojima, N. Tanaka, Cancer detection using infrared hyperspectral imaging, *Cancer Sci.* 102 (2011) 852–857. <https://doi.org/10.1111/j.1349-7006.2011.01849.x>.
  - [50] Y.H. El-Sharkawy, Optical Properties of Non-Malignant and Malignant Breast Tissue Determined by Surface Displacement of Laser-Induced Photoacoustic Generation, *Int. J. Opt. Photonic Eng.* 1 (2016) 1–8. <https://doi.org/10.35840/2631-5092/4502>.
  - [51] D.M. Schuster, P.T. Nieh, G.Z. Chen, Hyperspectral imaging and quantitative analysis for prostate cancer detection, (2020). <https://doi.org/10.1117/1.JBO.17.7.076005>.
  - [52] M. Halicek, H. Fabelo, S. Ortega, G.M. Callico, B. Fei, In-vivo and ex-vivo tissue analysis through hyperspectral imaging techniques: Revealing the invisible features of cancer, *Cancers (Basel)*. 11 (2019) 1–30. <https://doi.org/10.3390/cancers11060756>.
  - [53] P.-C. Chen, W.-C. Lin, Spectral-profile-based algorithm for hemoglobin oxygen saturation determination from diffuse reflectance spectra, *Biomed. Opt. Express*. 2 (2011) 1082–1096.
  - [54] W.A. Eaton, L.K. Hanson, P.J. Stephens, J.C. Sutherland, J.B.R. Dunn, Optical spectra of oxy- and deoxyhemoglobin, *J. Am. Chem. Soc.* 100 (1978) 4991–5003.
  - [55] V. V Tuchin, Tissue # Optics # and # Photonics # Biological # Tissue # Structures #, 1 (2015) 3–21.
  - [56] A. Rehman, I. Ahmad, K. Rehman, S. Anwar, S. Firdous, M. Nawaz, Optical properties measurement of highly diffusive tissue phantoms for biomedical applications, *Laser Phys.* 25 (2014) 25605.
  - [57] V. Tuchin, Tissue Optics and Photonics: Light-Tissue Interaction II, *J. Biomed. Photonics Eng.* 2 (2016) 030201. <https://doi.org/10.18287/jbpe16.02.030201>.
  - [58] P.C. Benias, D.L. Carr-Locke, Principles of Electrosurgery, *Ercp*. (2019) 86-92.e1. <https://doi.org/10.1016/b978-0-323-48109-0.00011-0>.
  - [59] T. Adão, J. Hruška, L. Pádua, J. Bessa, E. Peres, R. Morais, J.J. Sousa, Hyperspectral imaging: A review

- on UAV-based sensors, data processing and applications for agriculture and forestry, *Remote Sens.* 9 (2017). <https://doi.org/10.3390/rs9111110>.
- [60] S.S.M. Noor, K. Michael, S. Marshall, J. Ren, Hyperspectral image enhancement and mixture deep-learning classification of corneal epithelium injuries, *Sensors* (Switzerland). 17 (2017). <https://doi.org/10.3390/s17112644>.
- [61] V. Kumar, P. Gupta, Importance of Statistical Measures in Digital Image Processing, *Int. J. Emerg. Technol. Adv. Eng.* 2 (2012) 56–62.
- [62] S. Golestan, M. Ramezani, J.M. Guerrero, S. Member, F.D. Freijedo, Moving Average Filter Based Phase-Locked Loops : Performance Analysis and Design Guidelines, 29 (2014) 2750–2763.
- [63] H. Wu, L.R. Wilkins, N.P. Ziats, J.R. Haaga, A.A. Exner, Real-time monitoring of radiofrequency ablation and postablation assessment: Accuracy of contrast-enhanced US in experimental Rat liver model, *Radiology.* 270 (2014) 107–116. <https://doi.org/10.1148/radiol.13121999>.
- [64] A.L. Abdel Gawad, Y.H. El-Sharkawy, A.F. El-Sherif, Classification of human teeth caries using custom non-invasive optical imaging system, *Lasers Dent. Sci.* 1 (2017) 73–81. <https://doi.org/10.1007/s41547-017-0008-x>.
- [65] A.U. Hines-Peralta, N. Pirani, P. Clegg, N. Cronin, T.P. Ryan, Z. Liu, S.N. Goldberg, Microwave ablation: results with a 2.45-GHz applicator in ex vivo bovine and in vivo porcine liver, *Radiology.* 239 (2006) 94–102.
- [66] R. Hoffmann, P.L. Pereira, C.D. Claussen, S. Clasen, Comparison of Four Microwave Ablation Devices : An Experimental Study in ex Vivo Bovine Liver 1, 268 (2013).
- [67] F. Colletini, H. Rathke, B. Schnackenburg, A. Thomas, L. Albrecht, B. Suttmeier, M. Jonczyk, F. Guettler, B. Hamm, U. Teichgräber, Fluid preinjection for microwave ablation in an ex vivo bovine liver model assessed with volumetry in an open MRI system, *Diagnostic Interv. Radiol.* 19 (2013) 427.
- [68] G. Mauri, L. Cova, S. De Beni, T. Ierace, T. Tondolo, A. Cerri, S.N. Goldberg, L. Solbiati, Real-Time US-CT / MRI Image Fusion for Guidance of Thermal Ablation of Liver Tumors Undetectable with US : Results in 295 Cases, (2015) 143–151. <https://doi.org/10.1007/s00270-014-0897-y>.



**Mohamed Hisham Aref** is PhD Candidate at Military Technical College, Biomedical Engineering department. He received his BS degree in Biomedical Engineering from Military Technical College in 2006 and his MSc degree from Cairo University, Faculty of engineering in 2012, respectively; He is highly skilled & talented biomedical engineer with more than 14 years of practical experience in the design & improvement of the medical equipment's disease diagnosis, treatments & preventions. His current PhD topic in "*Monitoring & Control of Tumor Thermal Ablation using Advanced Imaging Technologies*". His current research interests include Hyperspectral Camera, Thermal Ablation, US imaging technologies, Cancer Early detection, Medical Gases Design, Hyperbaric Oxygen Therapy. He is a member of IEEE.



**Ibrahim H. Aboughaleb** is PhD Candidate at Military Technical College, Biomedical Engineering department. He received his BS degree in Biomedical Engineering from Military Technical College in 2006 and his MS degree from Cairo University, Faculty of engineering in 2014, respectively, Strong research professional and Experienced Biomedical Engineer with a demonstrated history of working in the hospital & health care industry.



Skilled in Medical Devices, Biomedical Electronics, Management, Circuit Analysis, and Biomedical Engineering.



**Yasser H. El-Sharkawy** is professor and Head of Biomedical Engineering department at Military Technical College. He received his BS and MS degrees in physics from the University of Optics in 1993 and 1996, respectively, and his PhD degree in optics from the Institute of Laser and Technology in 2006. He is the author of more than 54 journal papers. His current research interests include photo acoustic imaging used for breast cancer detection, Biophysics and Medical Physics, Medical Imaging and analysis, Biomedical Engineering.

Real-time Imaging Technique for Thermal Ablation	Thermal ablation Method	Subject of study	Ablation protocol	Ablation diameter	Ablation Volume
Gross Pathology (GP) [65,66]	MWA <sup>1</sup>	13 bovine 108 ablations	50–150 W 4–20 min	3.0 × 3.5–7.6 × 12.3	16.5–372.0 <sup>a</sup>
Magnetic Resonance Imaging (MRI) [67]	MWA <sup>2</sup>	50 cuboid bovine	45 W 7 min	--	7.3±2.1 4.7±1.6
Computerized Tomography (CT) [34]	MWA <sup>3</sup>	3 porcine	100 W 4.5 min	4.1±0.2×5.6±0.2	49.29 <sup>a</sup>
Ultrasonography (US) and Computerized Tomography (CT) [35]	MWA <sup>4</sup>	4 calf livers	50 W 10 min	2.1±0.1mm (15 markers used)	--
Contrast Enhanced Ultrasonography (CEUS) [36]	ILTT	12-patient clinical trial	15 W, 100 °C, 12 min	11~16 mm	1.2 <sup>a</sup> cm <sup>3</sup>
Real-Time US-CT/MRI Fusion [68]	RFA MWA <sup>5</sup>	987 patients (1,581 tumors-295 liver tumors)	50–150 W 4–20 min	16 of 295 (5.4 %) tumors were unsuccessfully completely ablated	--
Our proposed system	RF generator	10 ex-vivo bovine liver	50 W 3~5 min	1.69±0.1	22.35 <sup>a</sup>

**Table 1-** Summarize Table for Studies of Real-time Imaging modalities for ex-vivo Thermal Ablation; **GP** Gross Pathology; **MWA<sup>1</sup>** Microwave Ablation (AngioDynamics, Acculis MTA, F=2.45 GHz); **a** estimated volume; **MRI** Magnetic Resonance Imaging; **MWA<sup>2</sup>** (Medtronic, Evident™ Medtronic, F=915 MHz); **CT** Computerized Tomography; **MWA<sup>3</sup>** (HS Medical, Amica™, F=2.45 GHz); **MWA<sup>4</sup>** Microwave Ablation (KY-2000, Kangyou Medical, F=2.45 GHz); **CEUS** Contrast Enhanced Ultrasonography; **ILTT** Interstitial laser thermal therapy; **RFA** Radio-Frequency Ablation (Covidien, Boulder, CO); **MWA<sup>5</sup>** Microwave Ablation (AMICA, HS Hospital Service, Aprilia ;140 W, 2.45 GHz) ; **RF generator** (BOWA; Arc303, F= 9 kHz to 400 GHz).